Electronic Supplementary Material (ESI) for Journal of Materials Chemistry A.

## Supporting Information

# Iridium nanohollows with porous walls for acidic water splitting

## Experimental Materials

### *Chemicals*

Iridium (III) chloride hydrate ($IrCl_3 \cdot xH_2O$, 99.9%, Alfa Aesar) and citric acid (CA, $C_6H_8O_7$, 98%, Alfa Aesar) were purchased from J&K Scientific Ltd. Benzyl alcohol ($C_7H_8O$, analytical purity), glyoxal (GO, $C_2H_2O_2$, 40% aqueous solution, chemical purity) and ethanol ($C_2H_5OH$) were purchased from Sinopharm Chemical Reagent Co., Ltd. Cobalt acetylacetonate ($Co(acac)_3$) and Nafion® perfluorinated resin solution (5%) were purchased from Sigma-Aldrich.

### *Synthesis of Ir p-NHs*

In a typical synthesis of Iridium porous nanohollows (Ir p-NHs), $IrCl_3$ (6 mg) was dissolved in benzyl alcohol (6 mL) under sonication for 1 h. Then, CA (48 mg) and $Co(acac)_3$ (5 mg) were added into the above solution, followed by ultrasonication for another 0.5 h. Afterwards, 600 μL GO was added and the mixture was magnetically stirred for 10 min until a homogeneous solution was formed. After that, the dark green solution was transferred into a Teflon-sealed autoclave (25 ml) and maintained at 200 $^{o}C$ for 5 h. The resulting black product was collected by centrifugation and washed for six times with ethanol.

### *Characterizations*

Scanning electron microscopy (SEM) analysis was performed on a Zeiss Ultra-55 microscope, 5kV. Transmission electron microscopy (TEM) images and high-angle annular dark-field scanning TEM (HAADF-STEM) were collected by a JEOL-2011 at an accelerating voltage of 200 kV. The X-ray photoelectron spectra (XPS) was conducted on an Escalab 250Xi spectrometer and the data was calibrated with the C 1s peak at 284.5 eV. The concentration of catalysts was determined by the ICP-AES (710-ES, Varian, ICP-AES).

### *Electrochemical measurements*

HER and OER measurements were conducted on a CHI660 electrochemical workstation (Chenhua Instruments Co., Ltd.) with a typical three-electrode configuration. A graphite rod and a $Hg/Hg_2SO_4$ (filled with saturated $K_2SO_4$) electrode was used as the counter electrode and the reference electrode respectively. 0.5 M $H_2SO_4$ (pH=0.3) solution was used as electrolyte in this study. As-synthesized Ir p-HNs (1 mg) and Ketjen Black-300J support (1 mg) were dispersed in ethanol (10.0 mL) by sonicating for at least 2 h. After washing with ethanol and centrifugation for three times, the solid sample was collected by centrifugation and dried, and used as catalyst powder. For the catalyst ink preparation, the catalyst powder was dispersed in a mixture solution containing 490 μL ethanol and 10 μL Nafion, and ultrasonically mixed for 30 min. 10 μL of the suspension was cast onto a rotating glassy carbon electrode (GCE, a diameter of 5 mm), and dried under ambient conditions. Commercial 20 wt% Ir/C was used as benchmark, and 2 mg Ir/C was used to prepare the catalyst ink. The catalyst loading was kept as 0.2 $mg/cm^2$ for all samples. All the potentials are given against the reversible hydrogen electrode (RHE), converted by the Nernst equation. The scan rate of the linear sweep voltammetry (LSV) was set to be 5 mV/s. 50 cycles of fast CVs (100 mV $s^{-1}$) were recorded to stabilize the catalyst surface before collecting the LSVs. All polarization curves were given after iR correction for 95%. Electrochemical impedance spectra (EIS) were collected over the frequency ranging from 100 kHz to 0.01 Hz. Accelerated durability tests were conducted by cycling between 1.4 V and 1.55 V versus RHE at 100 mV/s for 4,000 cycles. The overall water splitting test were measured in a two-electrode cell using two identical Ir p-NHs electrodes, and carbon paper (CP) was used as the carrier with catalyst loading of 0.5 mg $cm^{-2}$. The stability measurements were conducted by long-term amperometric i-t curves.

### *DFT calculations*

All density functional theory (DFT) calculations were performed with the Vienna Ab Initio Simulation Package (VASP) code[1, 2]. The exchange correlation energy was modelled by using Perdew-Burke-Ernzerhof (PBE) functional within the generalized gradient approximation (GGA)[3]. The projector augmented wave (PAW)[4] pseudo-potentials were used to describe ionic cores. The cutoff energy of 500 eV was adopted after a series of tests. A Methfessel-Paxton smearing of 0.05 eV to the orbital occupation was applied during the geometry optimization and for the total energy computations. In all calculations, the atoms at all positions have Hellmann–Feynman forces lower than 0.02 eV $Å^{-1}$ and the electronic iterations convergence was $10^{-5}$ eV using the Normal algorithm. A 4-layer (2×2) $IrO_2$ (110) supercells with a sufficient vacuum gap of 15 Å were built to simulate the ideal surface. Structural optimizations were performed on all slab models with a grid of ($4 \times 4 \times 1$) k-point. Point defects are created by removing Ir atoms from top layer of the slab model. O, OH and OOH are added on the top site of $IrO_2$ (110) surface to simulate the absorbed OER intermediates. During the adsorption calculations, the top two layers are fully relaxed while the other layers are fixed at the tested lattice positions. We calculated the OER activity along a *OH – *O – *OOH – $O_2$ mechanism[5].

$H_2O \rightarrow e^- + {}^*OH + H^+$ (1)

${}^*OH \rightarrow e^- + {}^*O + H^+$ (2)

${}^*OH + H_2O \rightarrow e^- + {}^*OOH + H^+$ (3)

${}^*OOH \rightarrow e^- + O_2 + H^+$ (4)

Reaction energies for reaction (1) – (4) are calculated by,

$$\Delta E_1 = E_{*OH} + E(H^+ + e^-) - E_{H_2O}$$

$$\Delta E_2 = E_{*O} + E(H^+ + e^-) - E_{*OH}$$

$$\Delta E_3 = E_{*OOH} + E(H^+ + e^-) - E_{*O} - E_{H_2O}$$

$$\Delta E_4 = 4.92 - \sum_{i=1,2,3} \Delta E_i$$

where $E_{*OH}$, $E_{*O}$ and $E_{*OOH}$ are the electronic energies of adsorption configurations; $E(H^+ + e^-)$ is calculated based on computing hydrogen electrode model[6]. During the adsorption calculations, the top two layers are fully relaxed while the other layers are fixed at the tested lattice positions.. The energy of water is calculated at 0.035 bars. All reaction energies on ideal or defective $IrO_2$ (110) surface are shown in Figure S18.

The theoretical overpotential is then calculated by

$$\eta^{theor} = \frac{max\{\Delta E_1, \Delta E_2, \Delta E_3, \Delta E_4\}}{1e} - 1.23V$$

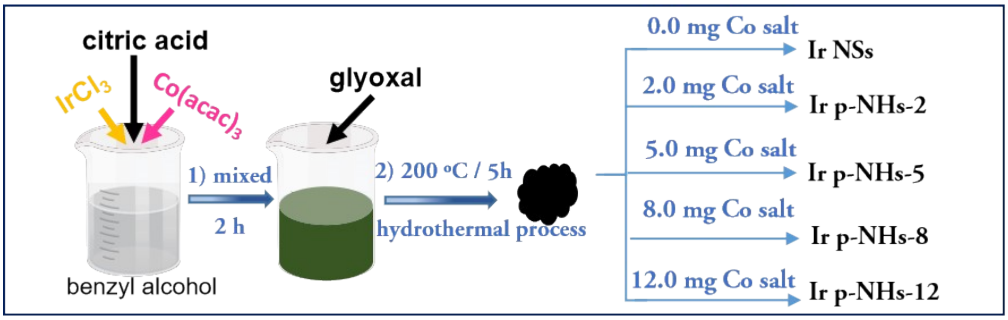

**Figure S1.** Synthetic procedure of Ir nanospheres (NSs) and porous nanohollows (p-NHs).

$$\mathrm{Ir} \rightleftarrows \mathrm{Ir}^{3+} + 3e^{-} \quad (E = 1.156\ \mathrm{V})$$

$$\mathrm{Co}^{3+} + e^{-} \rightleftarrows \mathrm{Co}^{2+} \quad (E = 1.82\ \mathrm{V})$$

$$\Longrightarrow \mathrm{Ir} + 3\mathrm{Co}^{3+} \rightleftarrows \mathrm{Ir}^{3+} + 3\mathrm{Co}^{2+} \quad (E = 0.664\mathrm{V})$$

**Figure S2.** Reactions involved in the Kirkendall process in this study, along with the corresponding standard reduction potentials.

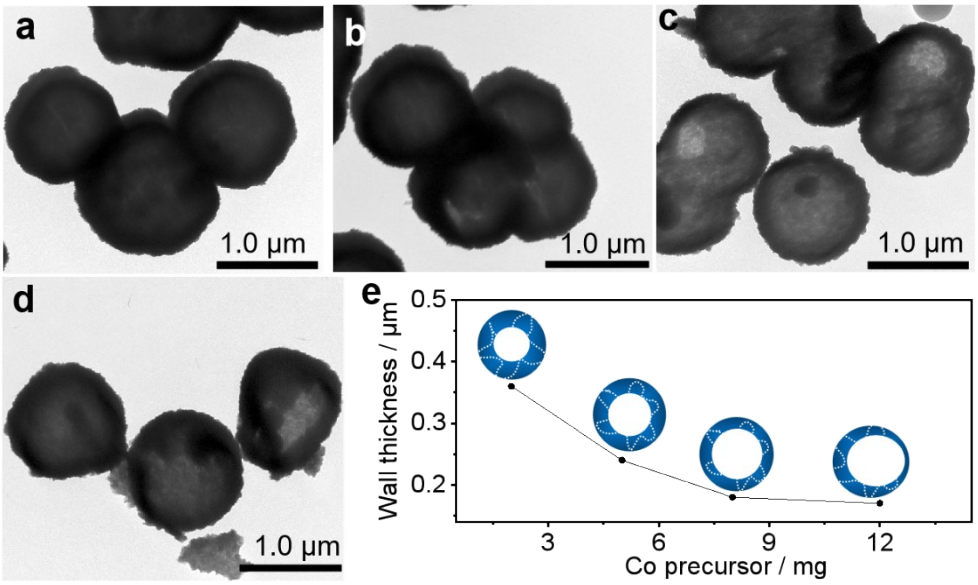

**Figure S3.** Dependence of wall thickness of nanohollows on the feeding amount of Co(acac)$_3$. TEM images of products with Co(acac)$_3$ of 2 mg (a), 5 mg (b), 8 mg (c) and 12 mg (d).

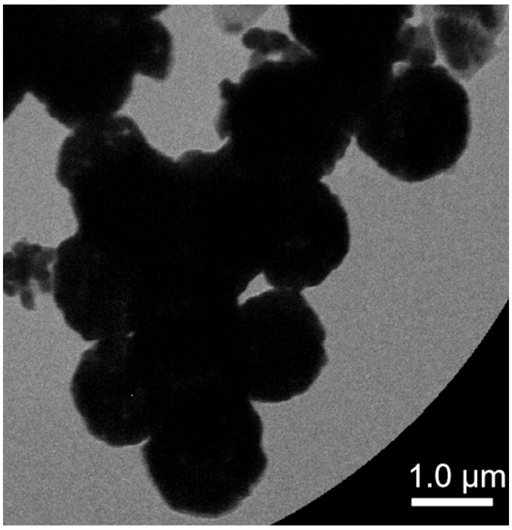

**Figure S4.** TEM image of product from identical synthetic conditions to p-NHs with the exception of Co(acac)$_3$ addition.

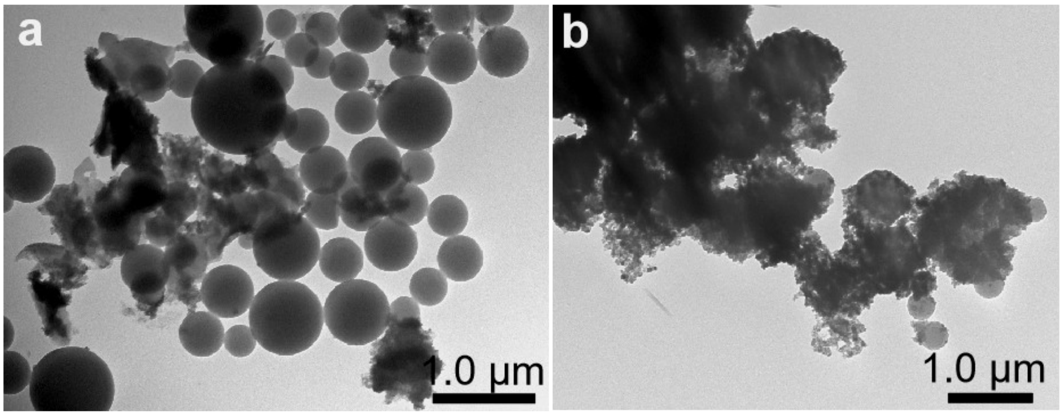

**Figure S5.** TEM images of products with identical recipe to p-NHs with the exception of (a) glyoxal and (b) citric acid.

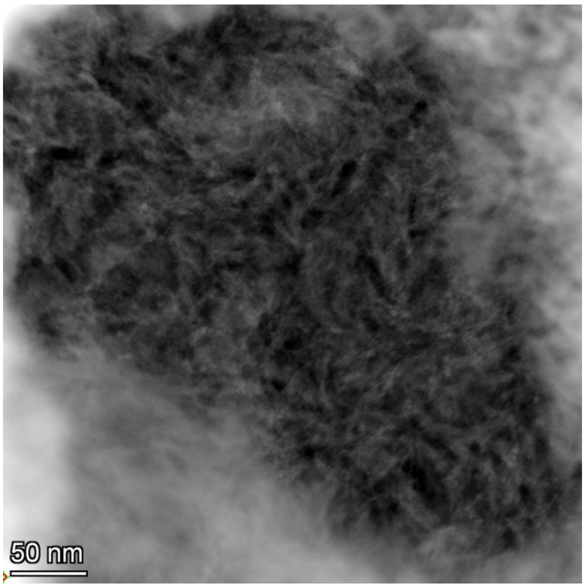

**Figure S6.** Top-view HAADF-STEM of Ir p-NHs.

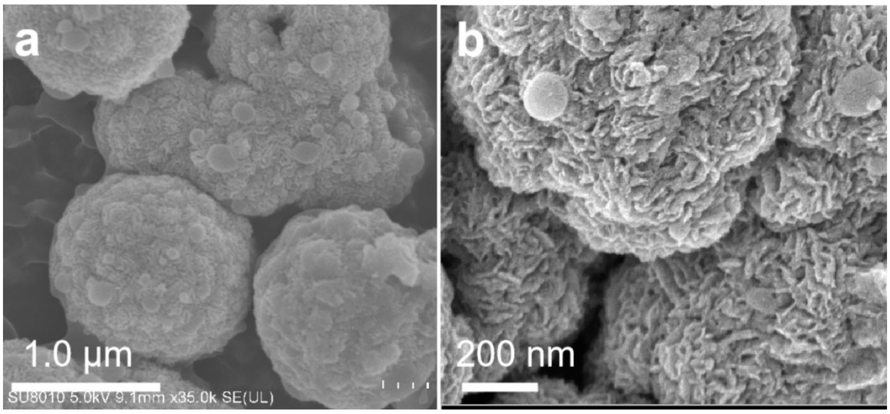

**Figure S7.** (a, b) Typical SEM images of Ir p-NHs.

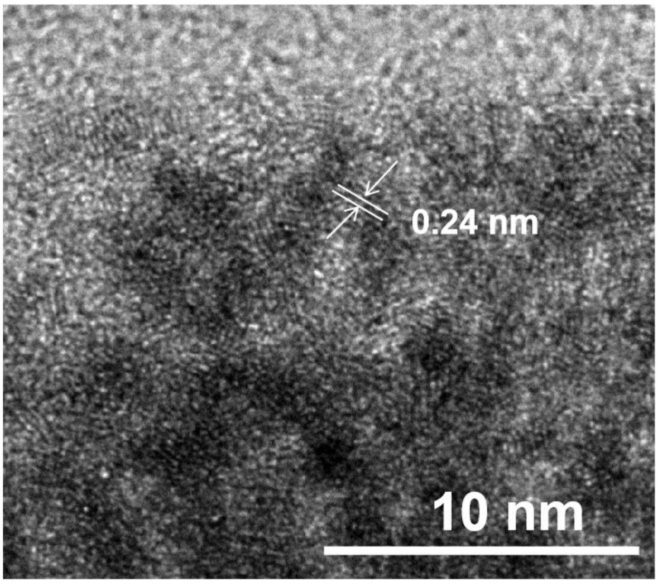

**Figure S8.** HRTEM image of Ir p-NHs.

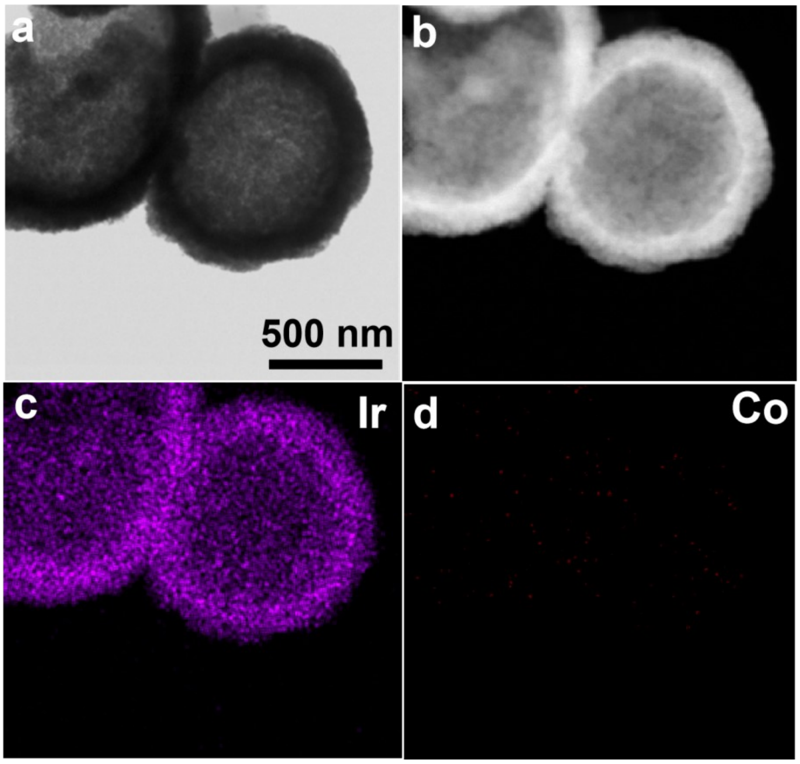

**Figure S9.** (a) HRTEM and (b) STEM image. (c and d) STEM-EDS elemental mappings of Ir p-NHs.

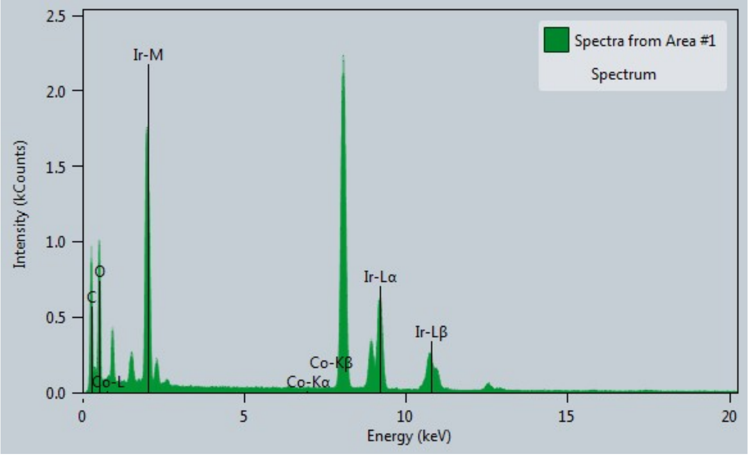

**Figure S10.** TEM-EDX spectrum of Ir p-NHs.

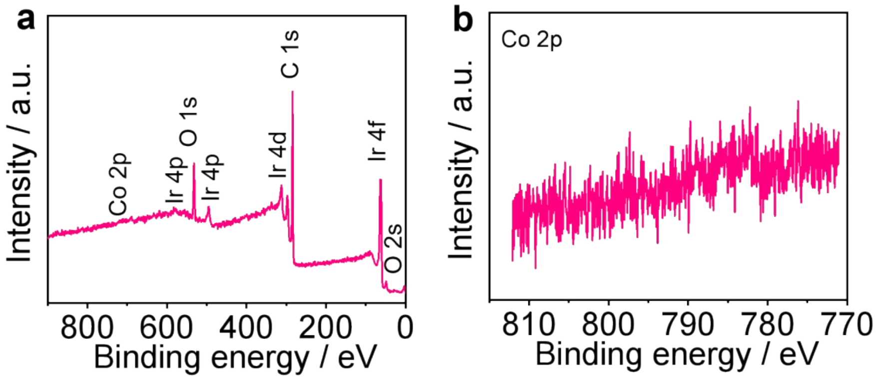

**Figure S11.** (a) XPS survey spectra and (b) Co 2p spectra of Ir p-NHs sample.

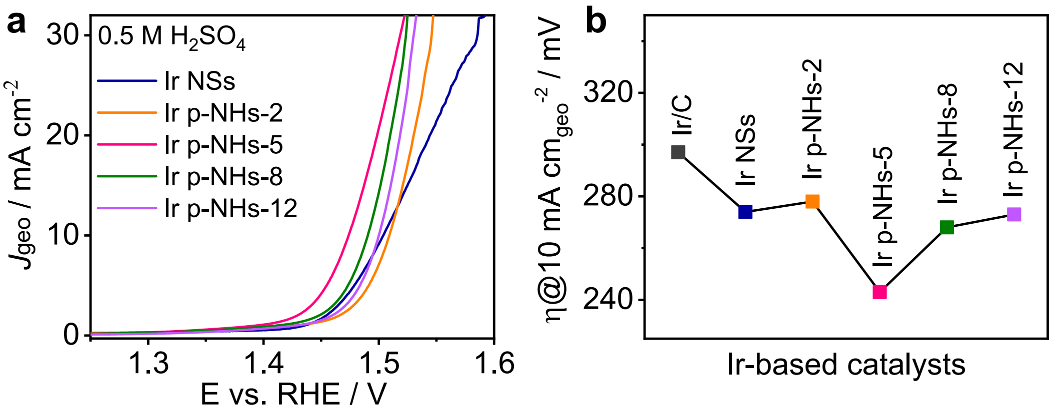

**Figure S12.** (a) Polarization curves and (b) overpotentials at 10 mA $cm^{-2}_{geo}$ of various Ir-based catalysts in 0.5 M $H_2SO_4$ solution, with currents being normalized to geometric surface areas.

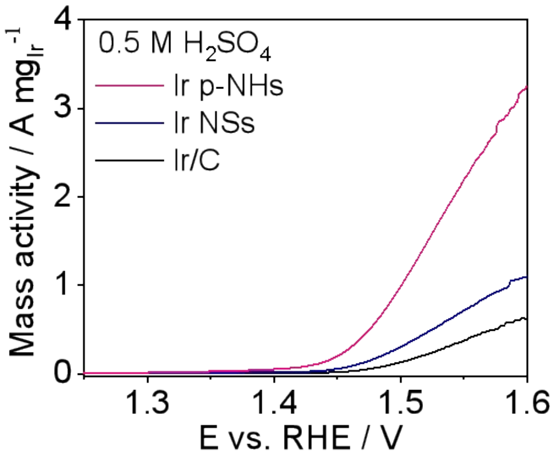

**Figure S13.** Mass activity (normalized to actual Iridium amount measured by ICP) of Ir p-NHs, Ir NSs and Ir/C as a function of potentials.

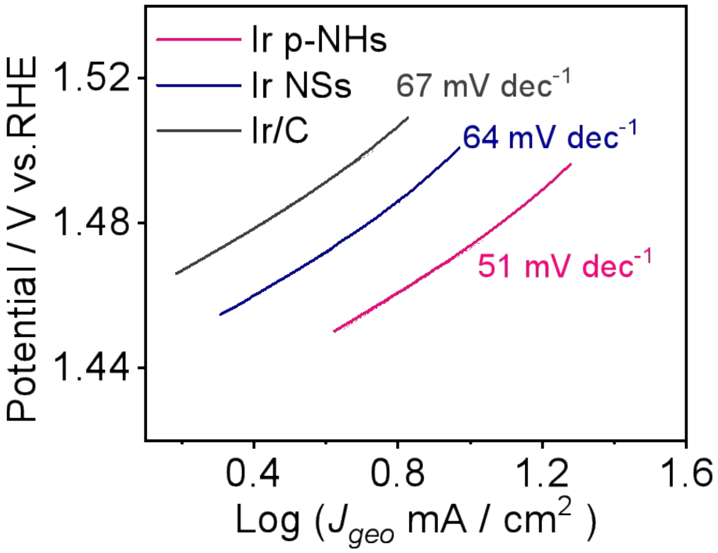

**Figure S14.** Tafel slope plots of various Ir-based catalysts in 0.5 M $H_2SO_4$.

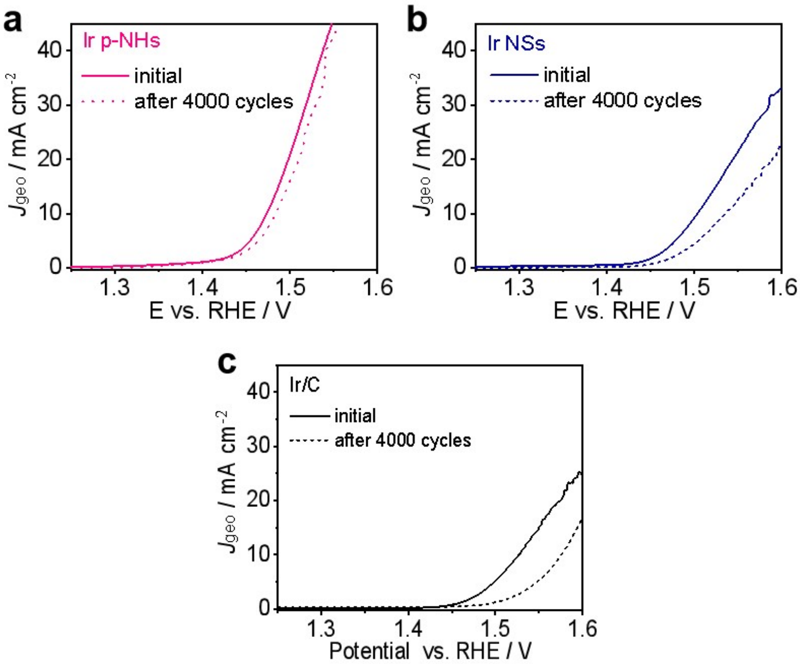

**Figure S15.** Polarization curves of Ir p-NHs, Ir NSs and 20wt% Ir/C before and after 4,000 cycles.

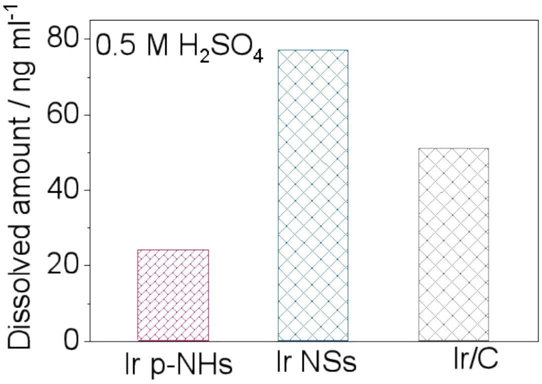

**Figure S16.** Amount of dissolved Ir from three anodes after OER cycling in 0.5 M $H_2SO_4$.

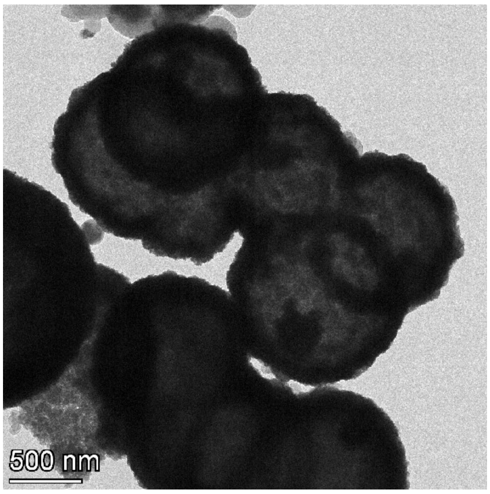

**Figure S17.** HRTEM images of Ir p-NHs after 10 h of overall water splitting test.

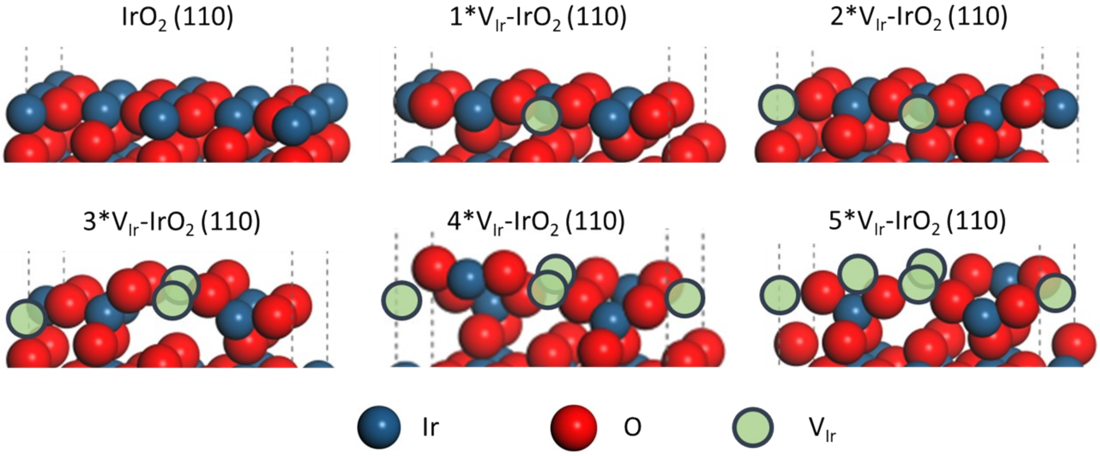

**Figure S18.** IrO$_2$ (110) surface models with different Ir vacancies.

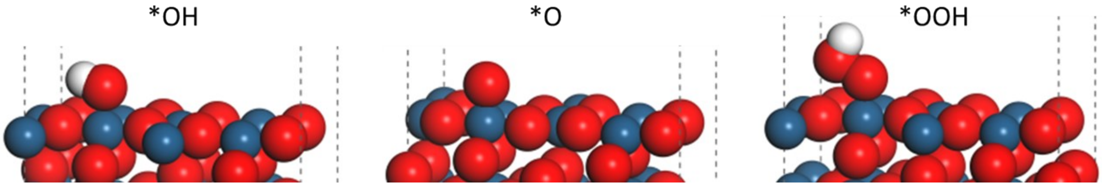

**Figure S19.** $IrO_2$ (110) surface models with different Ir vacancies.

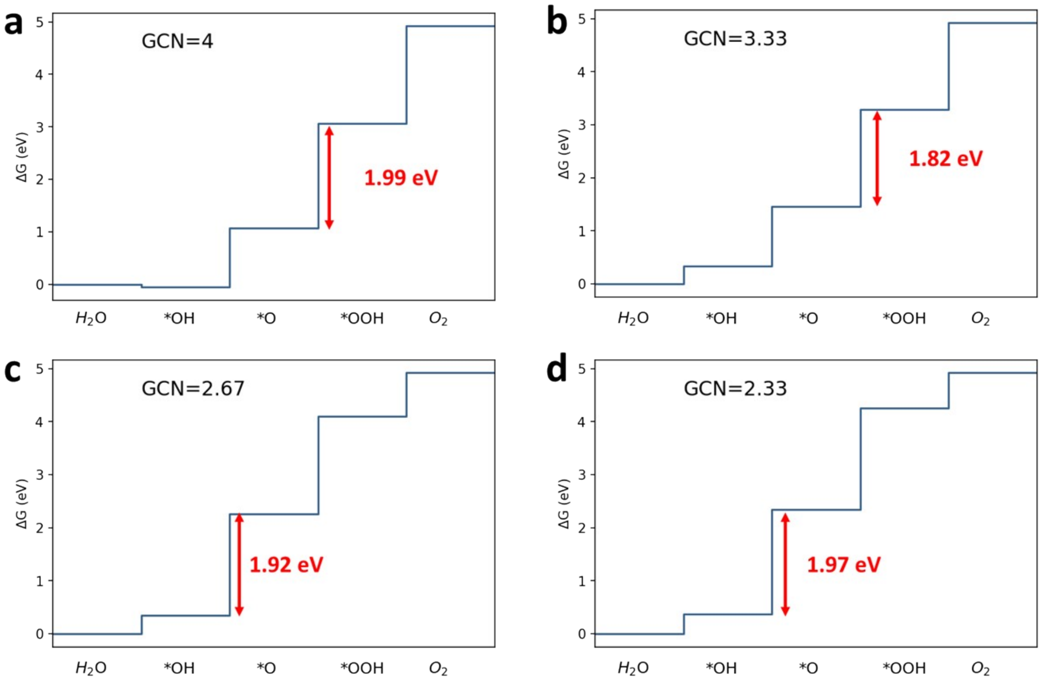

**Figure S20.** Reaction energy diagram of OER on defective $IrO_2$(110) surface with different GCN.

**Table S1.** Fit parameters for Ir 4f of Ir p-NHs and Ir NSs.

| **peak / eV** | $Ir^0$ $4f_{7/2}$ | $Ir^0$ $4f_{5/2}$ | $Ir^{4+}$ $4f_{7/2}$ | $Ir^{4+}$ $4f_{5/2}$ | $Ir^{4+}$ sat. | $Ir^{4+}$ sat. |
|---|---|---|---|---|---|---|
| **Ir p-NHs** | 61.04<br>(30.2%) | 61.70<br>(16.7%) | 64.04<br>(32.8%) | 64.70<br>(8.6%) | 62.50<br>(3.9%) | 65.54<br>(7.8%) |
| **Ir NSs** | 61.44<br>(23.2%) | 61.80<br>(18.6%) | 64.44<br>(21.4%) | 64.80<br>(14.0%) | 62.80<br>(11.4%) | 65.84<br>(11.4%) |

**Table S2.** Comparison of OER activities with recently reported monometallic Ir electrocatalysts in acidic electrolyte.

| **No.** | **Electrocatalysts** | $\eta_{10\ mA\ cm^{-2}}$ **/ mV** | **Electrolyte** | **References** |
|---|---|---|---|---|
| **0** | **Commercial Ir/C** | 297 | 0.5 M $H_2SO_4$ | Our work |
| **1** | **Ir p-NHs** | 243 | 0.5 M $H_2SO_4$ | |
| **2** | **Ir-IrOx/C-20** | 198 | 0.5 M $H_2SO_4$ | *J. Am. Chem. Soc.* **2022**, 144, 5, 2208–2217. |
| **3** | **Ir-NS** | 254 | 0.5 M $H_2SO_4$ | *Chem. Commun.*, **2021**, 57, 8620–8623. |
| **4** | **Ir-NSG** | 265 | 0.1 M $HClO_4$ | *Nat. Commun.* ***2020****, 11, 4246.* |
| **5** | **Ir-SA@Fe@NCNT** | 250 | 0.5 M $H_2SO_4$ | *Nano Letters* ***2020****, 20 (3), 2120-2128.* |
| **6** | **Li-IrOx** | 300 | 0.5 M $H_2SO_4$ | *J. Am. Chem. Soc.* **2019***, 141, 3014–3023.* |
| **7** | **1T-$IrO_2$** | 197 | 0.1 M $HClO_4$ | *Nat. Commun.,* ***2021****, 12, 6007.* |
| **8** | **Amorphous Ir NSs** | 255 | 0.1 M $HClO_4$ | *Nat. Commun. 10, 4855 (2019)* |
| **9** | **Ir-based nanocages** | 226 | 0.1 M $HClO_4$ | *Angew. Chem. Int. Ed.* ***2019****, 58 (22), 7244-7248* |
| **10** | **Ir nanoparticles on Ndoped graphene** | 303 | 0.5 M $H_2SO_4$ | *Nano Energy* ***2019****, 62, 117-126.* |
| **11** | **$IrO_x$/graphitic carbon nitride** | 276 | 0.5 M $H_2SO_4$ | *Angew. Chem. Int. Ed.* ***2019****, 58 (36), 12540-12544.* |

| | | | | |
|---|---|---|---|---|
| **12** | **$IrO_2$ nanoneedles** | 313 | 1.0 M $H_2SO_4$ | *Adv. Funct. Mater.* ***2018****, 28 (4), 1704796* |
| **13** | **Ir nanoparticles** | 290 | 0.5M HClO4 | *Inorg. Chem. Front.* ***2018****, 5 (5), 1121-1125.* |
| **14** | **Mesoporous metallic Ir nanosheets** | 240 | 0.5 M $H_2SO_4$ | *J. Am. Chem. Soc.* ***2018****, 140 (39), 12434-12441.* |
| **15** | **Ir WNWs** | 270 | 0.1 M $HClO_4$ | *Nanoscale,* **2018**, 10, 1892 |
| **16** | **Ir nanoparticles/ graphite foam** | 290 | 0.5 M $H_2SO_4$ | *Nano Energy* ***2017****, 40, 27-33.* |
| **17** | **Ir/GF** | 290 | 0.5 M $H_2SO_4$ | *Nano Energy* **2017**, 40, 27 |
| **18** | **IrOx/ATO** | 360 | 0.05 M $_2SO_4$ | *J. Am. Chem. Soc.* ***2016****, 138 (38), 12552-63* |
| **19** | **3D Ir superstructures** | 276 | 0.1 M $HClO_4$ | *Nano Lett* ***2016****, 16 (7), 4424-30* |

**Table S3** Quantitative GCN by creating different number of Ir defects.

| Number of surface Ir vacancies | GCN |
|---|---|
| **0** | **4** |
| **1** | **3.67** |
| **2** | **3.33** |
| **3** | **3** |
| **4** | **2.67** |
| **5** | **2.33** |

# Reference

1. Kresse G, Hafner J. Ab initio molecular dynamics for liquid metals. *Physical Review B* 1993, **47**(1)**:** 558.
2. Kresse G, Furthmüller J. Efficiency of ab-initio total energy calculations for metals and semiconductors using a plane-wave basis set. *Computational materials science* 1996, **6**(1)**:** 15-50.
3. Perdew JP, Burke K, Ernzerhof M. Generalized gradient approximation made simple. *Physical review letters* 1996, **77**(18)**:** 3865.
4. Kresse G, Joubert D. From ultrasoft pseudopotentials to the projector augmented-wave method. *Physical review b* 1999, **59**(3)**:** 1758.
5. Man IC, Su HY, Calle-Vallejo F, Hansen HA, Martínez JI, Inoglu NG*, et al.* Universality in oxygen evolution electrocatalysis on oxide surfaces. *ChemCatChem* 2011, **3**(7)**:** 1159-1165.
6. Nørskov JK, Rossmeisl J, Logadottir A, Lindqvist L, Kitchin JR, Bligaard T*, et al.* Origin of the overpotential for oxygen reduction at a fuel-cell cathode. *The Journal of Physical Chemistry B* 2004, **108**(46)**:** 17886-17892.